

Biodegradability and Surface Chemistry of AZ31D Compared with AZ91 Magnesium Alloy in a Modified Simulated Body Fluid

Zhaohui Wen¹, Shurong Duan^{1,*}, Changsong Dai^{2,*}, Feixia Yang², Feng Zhang¹

¹ Department of Neuro intern, First Affiliated Hospital of Harbin Medical University, Harbin 150001, China

² School of Chemistry Engineering and Technology, Harbin Institute of Technology, Harbin 150001, China

*E-mail: duanshurongls@163.com; changsd@hit.edu.cn

Received: 14 September 2014 / Accepted: 17 October 2014 / Published: 28 October 2014

In a modified simulated body fluid (*m*SBF), biodegradability and surface chemistry of AZ31D compared with AZ91 were studied using electrochemical techniques and immersion test. A protective surface film made the corrosion rate (CR) decreased rapidly and then reach a stable stage with immersion time increasing from 1d to 24d. CR of AZ91 was significantly lower than that of AZ31D and Ca, P, Mg, Al and O were homogeneously distributed in the corrosion layers of AZ31D, while, inhomogeneously in AZ91 due to much more β -phase inhomogeneously distributed in AZ91 and only a little β -phase distributed in AZ31D. The micro-galvanic couple formed at the boundaries between the β phase and Mg matrix to accelerate the α phase corrosion. With immersion time increased, the remaining β phases of AZ91 gradually formed a tight barrier while a loosen one were in AZ31D. Scanning electron microscopy (SEM) with energy dispersive spectroscopy (EDS) and X-ray diffraction (XRD) analysis verified that amorphous calcium phosphate or magnesium calcium apatite has formed on the surfaces of AZ91 and AZ31D.

Keywords: Magnesium alloy, Biodegradability, corrosion rate, electrochemical test

1. INTRODUCTION

The magnesium (Mg) alloys used in biomedical materials have received much attention in recent years because of their excellent biodegradability, which afford an alternative biomedical materials for treating cardiovascular and bone disease and no infection observed during the postoperative follow-up [1]. In selecting suitable structural materials, in addition to considering the

mechanical properties and implant function of the material, there is a need to emphasize the biodegradable performance of various Mg alloys in vitro and in vivo[1]. There are already many studies investigating the in-vitro and in-vivo biodegradability of Mg alloys[2-4]. Unfortunately, the unsatisfactory biodegradable performance of Mg alloys has been a major obstacle to their further use, particularly for AZ31 and AZ91 Mg alloys. Only several studies have been investigated on the biodegradable behavior of AZ31 alloy and there is also a contradictory if AZ31 Mg alloy, just like AZ91, can be strongly influenced by the amount and distribution of the β phase through its “dual-role” effect[5-8]. The current research results[9-10]demonstrate that it is feasible to improve the biodegradable resistance by adjusting the morphology, volume fraction and distribution of second phases due to its dramatical affect to the biodegradable behavior of magnesium alloys. Understanding the in-vitro behavior of Mg is a key to tailor Mg in-vivo biodegradation.

In the previous study, the biodegradable behavior of three kinds of magnesium has been investigated [11], In order to further understand if the minor change of microstructure and composition influence the biodegradation process, in vitro studies and electrochemical tests have been carried out in this study to evaluate the degradation characteristics and the surface chemistry of AZ31D compared with AZ91 magnesium alloys and the associated mechanism in a modified simulated body fluid (*m*SBF).

2. MATERIALS AND METHODS

Commercial Mg alloys AZ31D and AZ91 (Baoding Dong Qi Magnesium Alloy Products Co., Ltd, Shenzhen, China) were used in this study. Nomenclature of the samples was used according to the American Society for Testing and Materials (ASTM) standard [12]. Their nominal compositions (wt. %) are listed in Table 1. The samples were cut into 10 mm×10 mm×10 mm and 10 mm×10 mm×5 mm coupons for the immersion test and the electrochemical test, respectively.

Table 1. Chemical compositions of purity Mg and AZ31D and AZ91 magnesium alloys

| Sample | Chemical compositions (wt.%) | | | | | | | |
|--------|------------------------------|------|------|-------|---------|-------|-------|---------|
| | AL | Zn | Mn | Cu | Ni | Fe | Si | Mg |
| AZ31D | 2.84 | 0.80 | 0.25 | ≤0.01 | ≤0.001 | ≤0.02 | ≤0.05 | Balance |
| AZ91 | 8.51 | 0.64 | 0.22 | ≤0.05 | ≤0.0004 | 0 | 0 | Balance |

In this study, the in vitro immersion test was carried out in the *m*SBF, which was maintained at the most common body temperature of 37.5±0.5 °C. The composition of the *m*SBF was referred to the previous studies [11,13]. The solution was buffered with 2-(4-(2-hydroxyethyl)-1-piperazinyl) ethanesulfonic acid (HEPES) to a physiological pH of 7.4.

Table 2. Chemical composition of the m-SBF [11,13]

| Reagents | Amount |
|--|--------|
| NaCl (g/L) | 5.403 |
| NaHCO ₃ (g/L) | 0.504 |
| Na ₂ CO ₃ (g/L) | 0.426 |
| KCl (g/L) | 0.225 |
| K ₂ HPO ₄ ·3H ₂ O (g/L) | 0.230 |
| MgCl ₂ ·6H ₂ O (g/L) | 0.311 |
| 0.2 M NaOH (mL/L) | 100 |
| HEPES ^a (g/L) | 17.892 |
| CaCl ₂ (g/L) | 0.293 |
| Na ₂ SO ₄ (g/L) | 0.072 |
| 1M NaOH (mL/L) | 15 |

^a HEPES= 2-(4-(2-hydroxyethyl)-1-piperazinyl) ethanesulfonic acid

For the immersion test, the coupons were polished with SiC paper up to 1000 grit, ultrasonically rinsed in acetone for 10 min, dried in warm flowing air and then weighed by a balance with an accuracy of 0.1 mg. Then the samples were immersed in the *m*SBF for 1, 2, 5, 8, 16, 20 and 24 days. At each time point, the samples were removed from the *m*SBF, rinsed with de-ionized water, dried in warm flowing air and then weighed. The mass variation was calculated (mass variation = (mass after immersion-mass before immersion)/surface area), and then the samples were immersed in a solution comprising 200 g L⁻¹ CrO₃ and 19 g L⁻¹ AgNO₃ for 10–15 min to remove the corrosion products. After that, they were quickly cleaned with distilled water, dried in warm flowing air and weighed for the final weight (mass loss = (mass after cleaning in chromic acid – mass before immersion)/surface area). Three parallel immersion tests were carried out for an average mass loss result.

The corrosion rate (CR, mm/yr) of the samples was calculated via the following equation[14]:

$$CR = \frac{8.76 \cdot 10^4 W}{AT\rho} \quad (1)$$

where *W* is the mass loss (g), *A* is the original surface area exposed to the corrosive media (cm²), *T* is the immersion time (h), and ρ is the sample standard density (g/cm³) (AZ91, 1.81 g/cm³, AZ31D, 1.77 g/cm³).

After the samples were mounted in epoxy-resin with only one surface of 1cm² exposed, the samples were polished with SiC paper up to 1000 grit, washed with distilled water and ultrasonically cleaned in acetone prior to the tests. The polarization experiments were performed using a Model 273 potentiostat (made by EG&G Princeton Applied Research). The electrochemical impedance spectroscopy (EIS) tests were carried out under different conditions at 37±0.5°C using a Model 273 potentiostat, a 5210 phase-lock amplifier, a NEC Power mate ITX computer system, and EG&G M 398 EIS testing system in a range of 0.1 Hz–10 kHz. The experimental setup was a standard three-

electrode system with the sample as the working electrode, saturated calomel electrode (SCE) as the reference electrode, and a platinum mesh as the counter electrode. The results of the measurements were analyzed by using the EG&G EQUIVCRT software. Prior to the beginning of the polarization and EIS experiments, the samples were first immersed in a beaker open to air containing the *mSBF* maintained at 37°C for 1 h to establish a relatively stable free corrosion potential. The sweep rate of the polarization curve measurement was 0.5 mVs⁻¹. The corrosion current density (i_{corr}) was converted into the corrosion rate according to the Faraday's Law.

$$\text{CR} = \frac{M i_{\text{corr}}}{n F \rho} \quad (2)$$

where CR* is the corrosion rate, M is the molar mass (magnesium: 24.31 g/mol), t equals to 3600*24*365s, i_{corr} is the corrosion current density, n is the number of electrons involved in the corrosion reaction, F is the Faraday's constant (96 485 As/mol), and ρ is the standard density of the Mg alloy.

Before and after the corrosion layers were cleaned, the surface morphology and the chemical compositions of the microstructure of the samples were examined with a scanning electron microscopy (SEM, HITACHI S570, S-4700, Japan) with energy dispersive spectroscopy (EDS). X-ray diffraction (XRD) with a powder X-ray diffractometer (Rigaku D/max- γ B, Japan) was performed to identify the crystalline phase of the materials after immersion into *mSBF* with Cu K α 1 (45 kV, 50 mA, step size=0.02°, 10°<2 θ <90°) radiation. The RAD-B qualitative analysis software was employed to calculate the percentages of the constituent phases of the deposit coatings from XRD peak intensity.

3. RESULTS AND DISCUSSION

3.1 Immersion tests

The SEM images of AZ31D and AZ91 Mg alloy are shown in Fig.1. After immersion into *mSBF* for different periods, four samples of AZ31D and AZ91 Mg alloy were investigated, respectively. Different samples of the same Mg alloy showed different corrosion appearance after immersion into *mSBF* for the same time due to the composition dispersed not absolutely uniform. After AZ31D and AZ91 were immersed into *mSBF* for 1d, only a little white substances was observed on the surfaces of AZ31D and little was observed on the surfaces of AZ91 of which a little pit emerged in one of the samples accompanied with H₂ generated. As time tended to 2d, A little corrosion pit emerged on the surfaces of part of AZ31D and AZ91 and trace of cotton-like substance on the bottom of the bottles. Most of H₂ generated in the serious corrosion site such as corrosion pits of AZ31D and AZ91 alloy. When the time increased to 5d, the obtained corrosion pit on most of the samples in AZ91 and AZ31D began to become deeper and deeper and the corrosion pits. With time increased, the pits of AZ31D became deeper and larger and the pits of AZ91 were shallower with some micropore (Fig.1(b)).

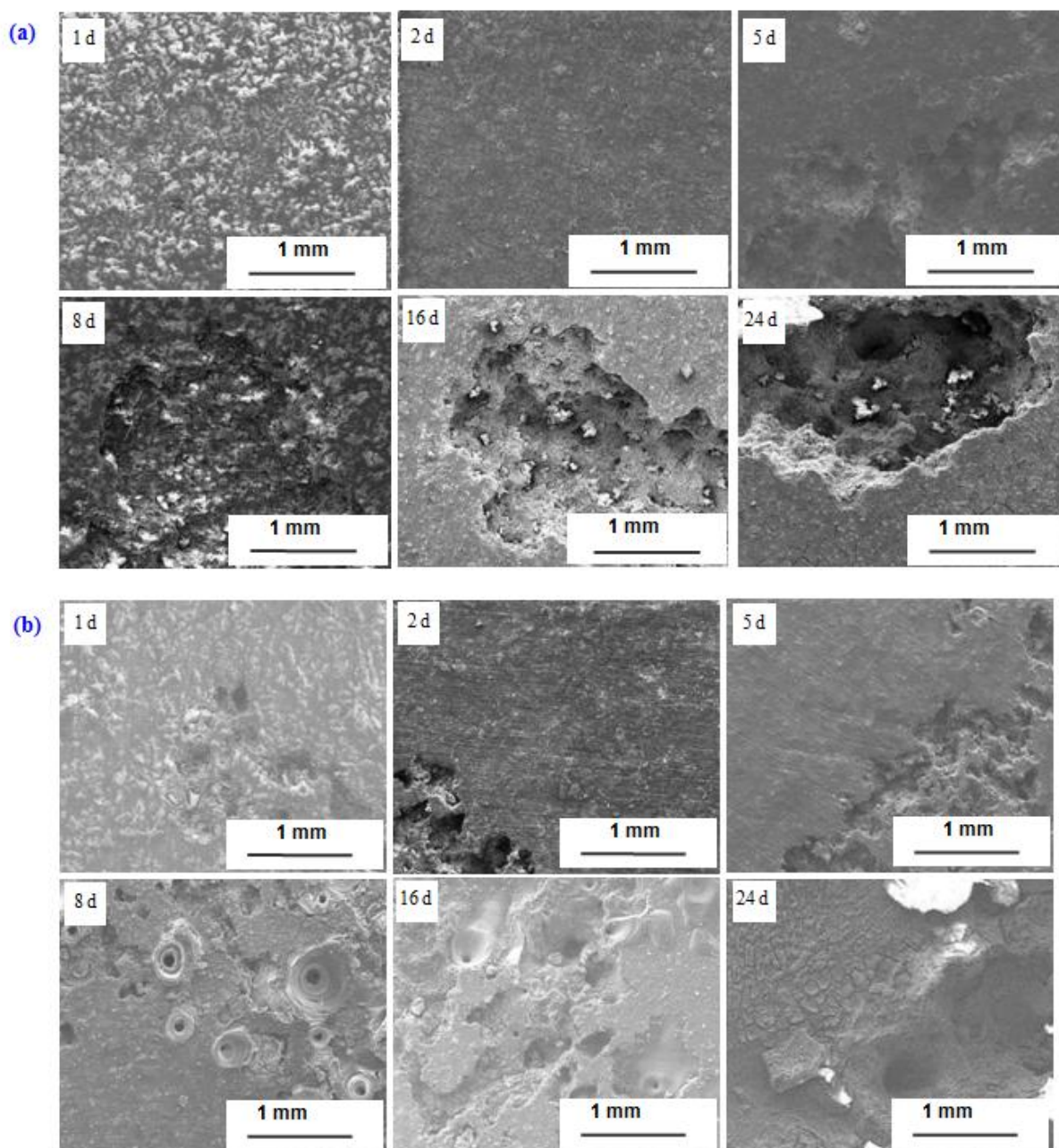


Figure 1. SEM micrographs of AZ31D(a) and AZ91(b) Mg alloys after immersion into the *mSBF* for 1d,2d,5d,8d,16d,24d.

EDX mappings of the elements detected in the corrosion layers of AZ31D and AZ91 Mg alloy after immersion into *mSBF* for 5 d are shown in Fig.2. Fig. 3 shows EDS of AZ31D and AZ91 Mg alloy after immersion into *mSBF* for 8 d. Fig.4 shows Ca/P ratio of AZ31D and AZ91 Mg alloy after immersion into *mSBF* for different time. After AZ31D and AZ91 immersed into *mSBF* for 5d, EDX mapping observed that Ca, P, Mg, Al and O were homogeneously distributed in the corrosion layers of AZ31D, while, inhomogeneously distributed in AZ91. The apparent cracks, peeling-off parts and corrosion products around the cracks were observed. EDS also revealed that AZ91 were composed of Al (18.71 at.%), Zn (1.67 at.%), and Mn (0.61 at.%) and AZ31D possessed Al (10.73 at.%), Zn

(8.17at.%) and Mn (2.97at.%) (Fig.3). It has also revealed that high concentrations of Ca, P, Mg, O elements were in the corrosion layers which might be Ca–P salts containing Mg and/or $Mg(OH)_2$ and the alloying elements were incorporated into the corrosion layers (Fig.2 and 3). The Ca/ P ratio plots of two kinds of samples showed increased tendency with time increased from 1d to 24d except AZ31D immersion time being 16d and AZ91 being 24d which might be due to the corrosion product peeling off from the surfaces (Fig.4). Over the whole immersion time, all Ca/P ratios were lower than 1.3.

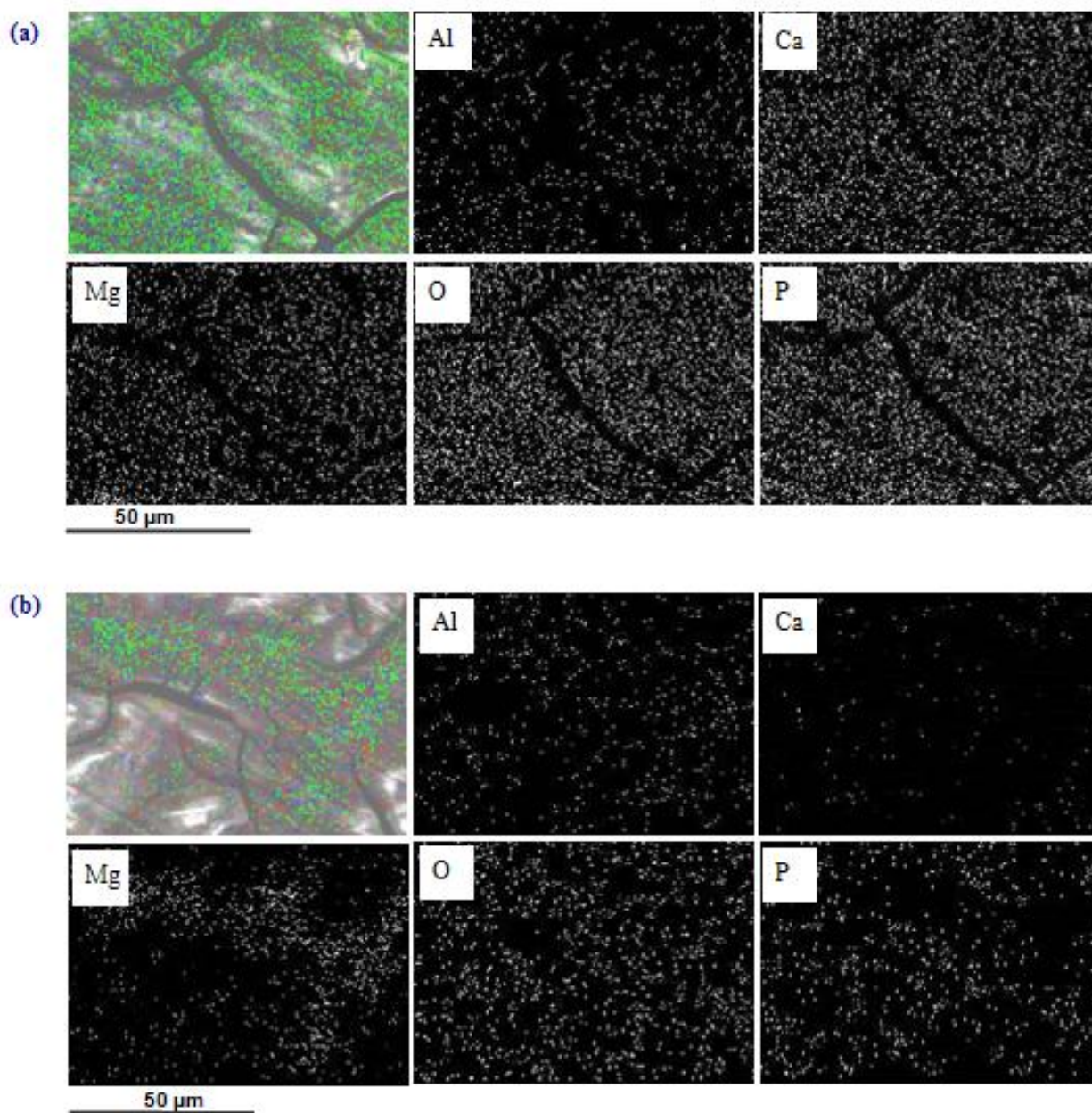


Figure 2. EDX mappings of the elements (Al, Ca, Mg, O, P) detected in the corrosion layers of AZ31D (a) and AZ91 (b) Mg alloys after immersion into the *m*SBF for 5 d.

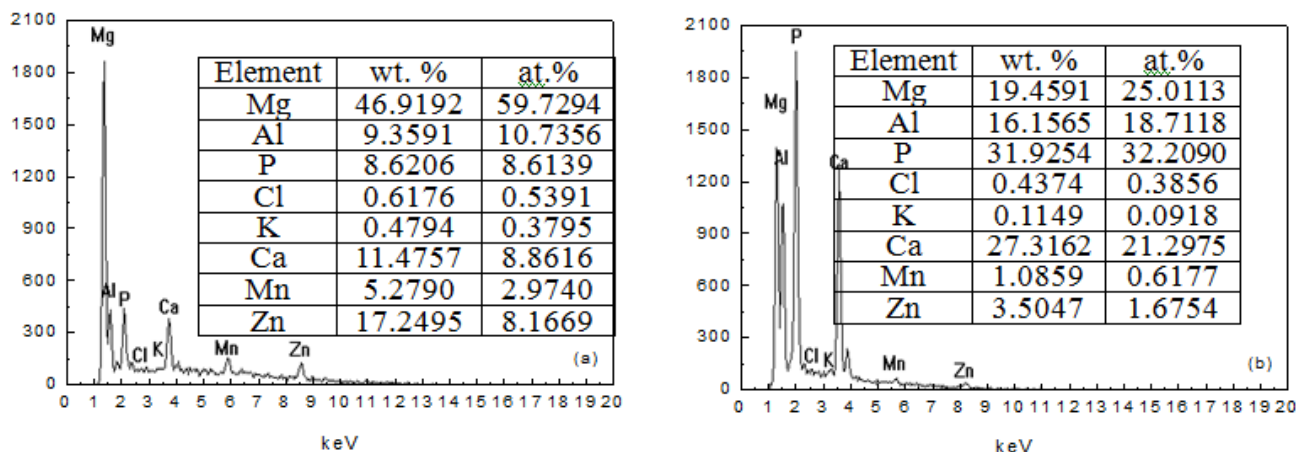


Figure 3. EDS of AZ31D and AZ91 Mg alloys after immersed into the *m*SBF for 8 d.

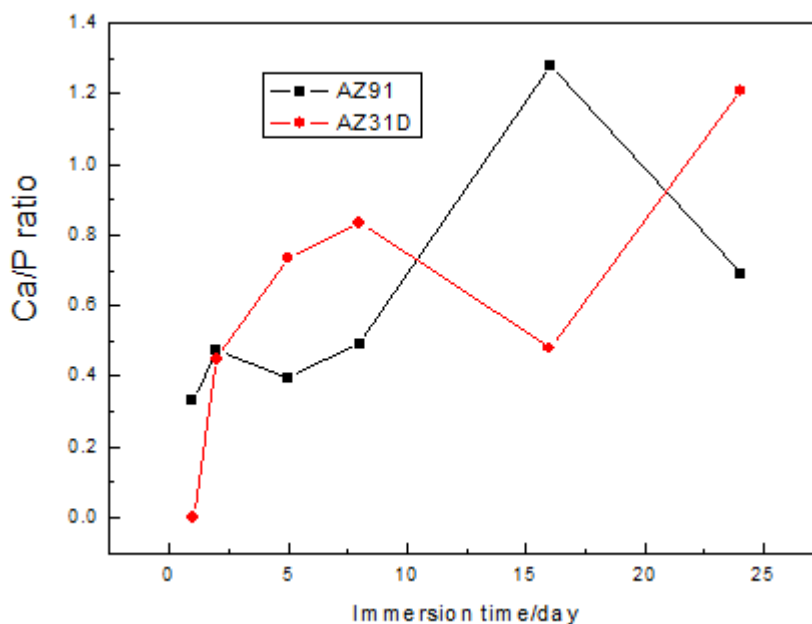


Figure 4. Ca/P ratio of AZ31D and AZ91 Mg alloys after immersed into the *m*SBF for 1d,2d,5d,8d, 16d, 24d.

Fig.5 shows XRD of AZ31D and AZ91 Mg alloys after immersion into the *m*SBF for different days. All the characteristic peaks originate from the protective film and metallic Mg substrate. The peaks in the XRD spectra of AZ31D related with $Mg_{0.97}Zn_{0.03}$, AZ91 corresponded to $Mg_{12}Al_{17}$ beside Mg element. However, $Mg(OH)_2$ and MgO phases were detected in the specimen. Besides, many small peaks were present in the 2θ range between $20-35^\circ$ which were most likely associated with amorphous calcium phosphate or magnesium calcium apatite ($Ca_{10-x}Mg_x(PO_4)_6(OH)_2$).

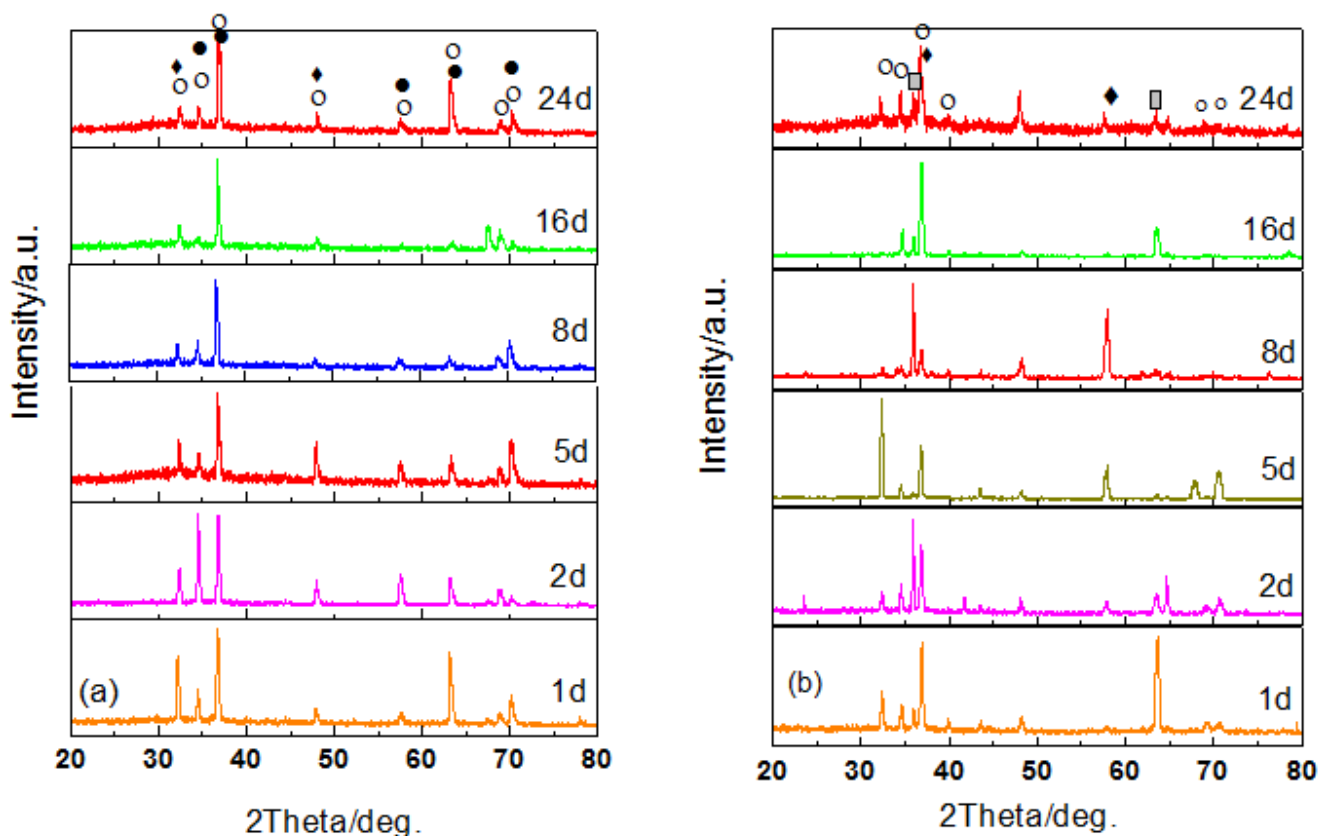


Figure 5. XRD spectra of AZ31D and AZ91 Mg alloys after immersion into the *mSBF* for 1d,2d,5d,8d,16d, 24d.(□Mg◆HA,■Mg₁₂Al₁₇ ●Mg_{0.97}Zn_{0.03})

Fig.6 shows the typical microstructures of AZ31D and AZ91 Mg alloy immersed into *mSBF* for 30d after the corrosion layers were removed. The surfaces of two kinds of samples were more like a foam of which AZ31D possessed different size of pits and showed more loosen and serious corrosion than that of AZ91 whose pits was more well-distributed(Fig.6). The pits of AZ91 Mg alloy were about 40μm in diameter within and they developed and connected resulting in the localized corrosion. In addition, it was found that the whole α grains undergo a majority of corrosion and the border of the corroded area was mostly surrounded by the β -phase. AZ91 formed a more tight grain boundaries than that of AZ31D. Moreover, the β -phase of AZ31D could act as a galvanic cathodic to accelerate pit propagation due to its divided and discontinuous microstructure. EDS analysis of AZ31D on different site of grain boundaries were analysed and showed that the plate-like particles were rich with element of Mg, Mn and Al which might be β -Mg₁₂Al₁₇ phase, Al₈Mn₅ phase and α -Mg(point 1 and 2 of Fig. 5(a), Table 3) and the left parts boundaries mainly consisted of Mg and a little Al and Zn (point 3 and 4 of Fig. 5(a), Table 3). While, the boundaries of AZ91 possessed more Al than that of AZ31D(point 1 and 2 of Fig. 5(b), Table 3) which were mainly β -Mg₁₂Al₁₇ phase. The angular shaped particles were rich of Mg and Mn, only a little Al and Zn were exist (point 5 of Fig. 10(b), Table 3) which were interpreted as Mn-rich[15]. Only less angular shaped particles emerged in the pit of AZ31D and much in that of AZ91. Mg element and little Al, Mn and Zn were in the pits of AZ31D and an α -Mg matrix

with coarse β -phase (β -Mg₁₂Al₁₇ phase) particles were in the pits of AZ91 alloy (point 6 of Fig. 6, Table 3).

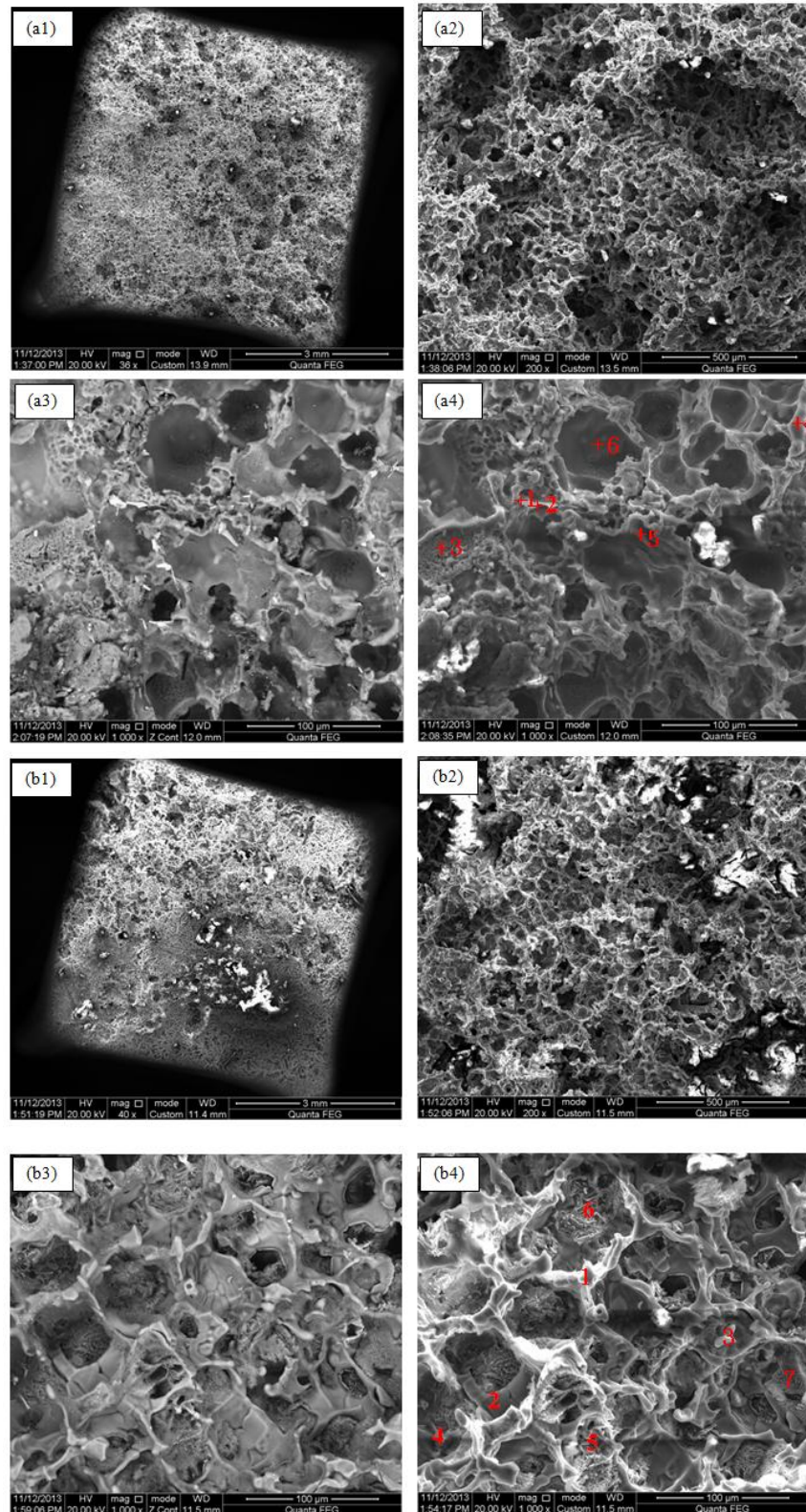


Figure 6. SEM of AZ31D and AZ91 Mg alloys after cleaning of the surface in chromic acid which were immersed in the *m*SBF for 30d.

Table 3. The EDS of AZ31D and AZ91 Mg alloy immersed into m-SBF for 30d after the corrosion layers were removed.

| Sample | Point | Phase | Chemical compositions (wt.%) | | | | Chemical compositions (at.%) | | | |
|--------|-------|--|------------------------------|-------|-------|-------|------------------------------|-------|-------|-------|
| | | | Mg | Al | Mn | Zn | Mg | Al | Mn | Zn |
| AZ31D | 1 | Mg ₁₂ Al ₁₇ +Al ₈ Mn ₅ | 43.12 | 29.71 | 25.70 | 1.47 | 52.71 | 32.72 | 13.90 | 0.67 |
| | 2 | Mg ₁₂ Al ₁₇ +Al ₈ Mn ₅ | 32.97 | 37.55 | 28.41 | 01.07 | 41.33 | 42.42 | 15.76 | 00.50 |
| | 3 | α | 92.99 | 05.09 | 00.56 | 01.35 | 94.57 | 04.67 | 00.25 | 00.51 |
| | 4 | α+Mg ₁₂ Al ₁₇ | 86.81 | 09.41 | 00.58 | 03.19 | 89.74 | 08.77 | 00.27 | 01.23 |
| | 5 | Mn | 53.91 | 2.48 | 40.96 | 2.65 | 71.64 | 2.97 | 24.08 | 1.31 |
| | 6 | α | 94.24 | 03.52 | 00.61 | 01.64 | 95.88 | 03.22 | 00.27 | 00.62 |
| AZ91 | 1 | Mg ₁₂ Al ₁₇ | 63.89 | 30.08 | 00.68 | 05.37 | 68.49 | 29.06 | 00.31 | 02.14 |
| | 2 | Mg ₁₂ Al ₁₇ | 57.76 | 37.77 | 00.63 | 03.84 | 61.78 | 36.40 | 00.30 | 01.53 |
| | 3 | Mg ₁₂ Al ₁₇ | 50.10 | 46.89 | 00.52 | 02.49 | 53.58 | 45.18 | 00.25 | 00.99 |
| | 4 | Al ₈ Mn ₅ +Mg ₁₂ Al ₁₇ | 15.07 | 52.52 | 31.53 | 00.88 | 19.6 | 61.72 | 18.20 | 00.43 |
| | 5 | Al ₈ Mn ₅ +Mn | 14.53 | 08.23 | 75.45 | 01.79 | 25.9 | 13.24 | 59.62 | 01.19 |
| | 6 | Mg ₁₂ Al ₁₇ | 60.20 | 37.12 | 00.37 | 02.31 | 63.59 | 35.33 | 00.17 | 00.91 |
| | 7 | α | 72.62 | 09.55 | 03.92 | 13.91 | 82.40 | 09.77 | 01.97 | 05.87 |

Fig.7.shows mass change and CR of AZ31D and AZ91 Mg alloys immersed in the mSBF before ((a): mass variation)) and after ((b): mass loss) cleaning of the surface in chromic acid. From Fig.7(a), it was observed that the mass variation plot of AZ31D alloy increased rapidly than that of AZ91 alloy. After immersion time increased from 1d to 16d, the mass variation of AZ31D alloy increased from 1.265 mg/cm² to 12.648 mg/cm².After immersion time changed from 16d to 24d, the mass variation kept stable and changed to 12.053 mg/cm². However, the tendency of the mass variation plot of AZ91 keep increased from -0.182 mg/cm² to 4.245 mg/cm² from 1d to 24d, except 20d(2.586mg/cm²).When the immersion time was 20d, the mass variation was lower than that of immersion time of 16d(3.514 mg/cm²)and 24d(4.245 mg/cm²). It was also observed that the plot of the mass loss showed a little different from that of the mass variation Fig.7 (b). After the corrosion products were removed, these plots became more sharper. The plots of AZ91 were more stable than that of AZ31D before and after cleaning of the surfaces.The conversion of the mass loss into corrosion rates revealed that CR of AZ31D was decreasing from 8.055mm/year to 2.520mm/year with immersion time increasing from 1d to 8 d. From 8d to 24d, the degradation rate became stable which decreased slightly from 2.520mm/year to 1.636mm/year. The CR plot of AZ91 kept much stable and lower than that of AZ31D during the whole immersion time. The CR of AZ91 was about 2.387mm/year after immersion time for 1d and then converted to 0.8858 mm/year with time increased to 24d Fig.7 (c).

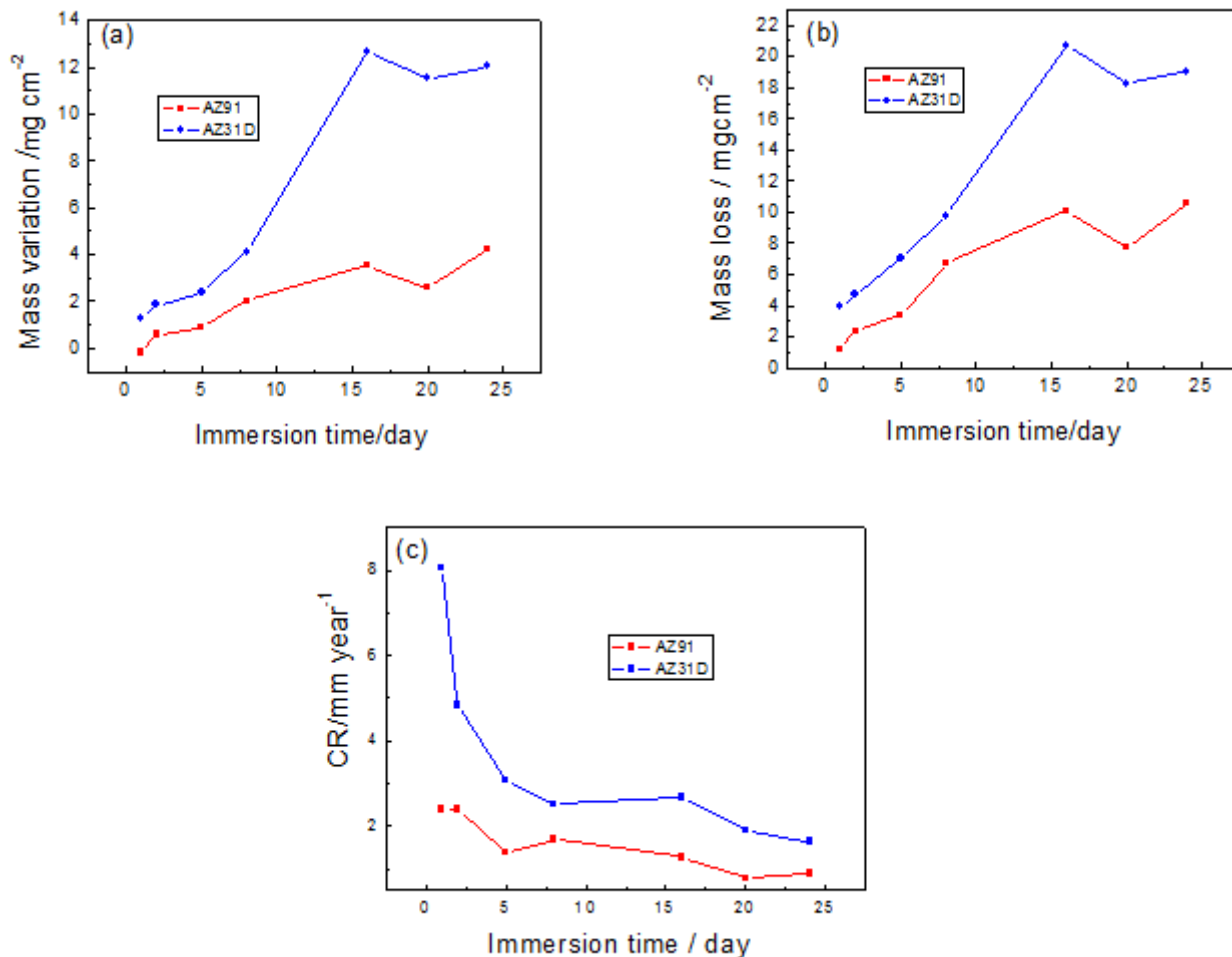


Figure 7. Mass changes of AZ31D and AZ91 Mg alloys immersed in the *mSBF* before ((a): mass variation)) and after ((b): mass loss) cleaning of the surface in chromic acid and CR(c) of AZ31D and AZ91 Mg alloys after immersion in the *mSBF* for 1d, 2d, 5d, 8d, 16d, 20,24d.

3.2 Electrochemical test

Fig.8 and Table 4 show the Nyquist plots and the equivalent circuit of AZ31D compared with AZ91 Mg alloys after immersion in the *mSBF* for different days. Fig.9 shows the R_p of AZ31D, compared with AZ91Mg alloys after immersion in the *mSBF* for different days. The diameter of the capacitive loop at the high frequency range reflects the charge transfer resistance (R_{ct}), and that at the medium one reflects the surface film resistance (R_f) and the low one represents the inductive loop[16]. Two capacitive loops were observed in the Nyquist plots of AZ31D and AZ91 alloy which were at a high frequency range and a mid frequency range. The inductive loop were emerged in AZ31D whose immersion time being 5d and AZ91 being 1d.

The equivalent circuit in Fig.9 was used for fitting EIS data with two and one capacitive loops presented in the plot of AZ31D and AZ91 alloys, where R_Ω is the ohmic solution resistance, Q_1 is the capacitance related to the electric double layer, Q_2 is the film capacitance corresponding to corrosion product[17,18]. The polarization resistance, R_p , is an important parameter, the reciprocal of which is

proportional to the corrosion rate. R_p can be calculated from the equivalent circuits by adding R_{ct} and R_f which suggested that AZ91 exhibited a higher degradation resistance than that of AZ31D at immersion time being 1d and 5d while lower one being 2d which might be due to the corrosion layers detached. R_p of AZ91 first decreased and then increased, while AZ31D first increased and then decreased (Fig.10).

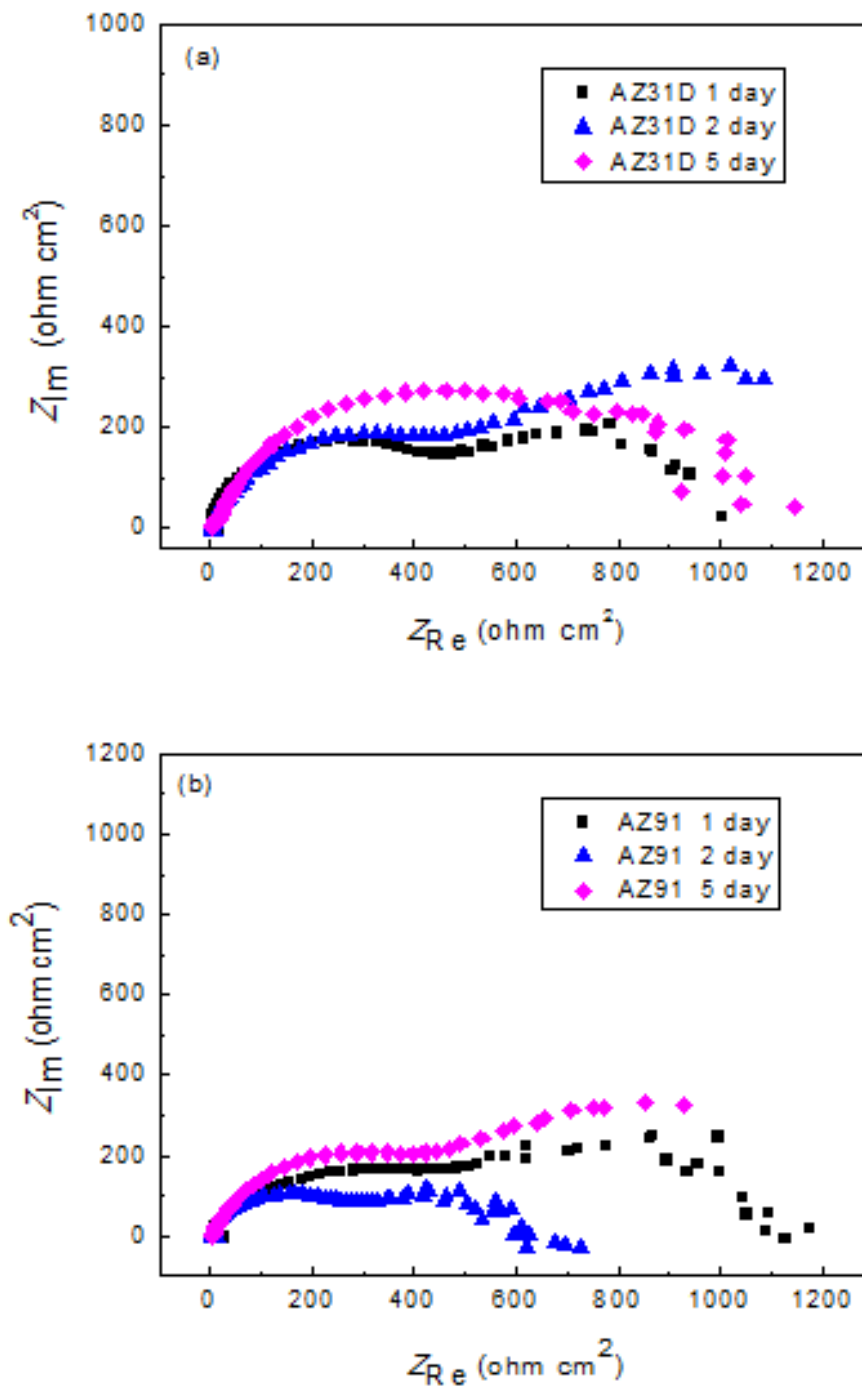


Figure 8. The Nyquist plots of AZ31D(a) and AZ91(b) Mg alloys after immersion in the *m*SBF for 1d, 2d and 5d.

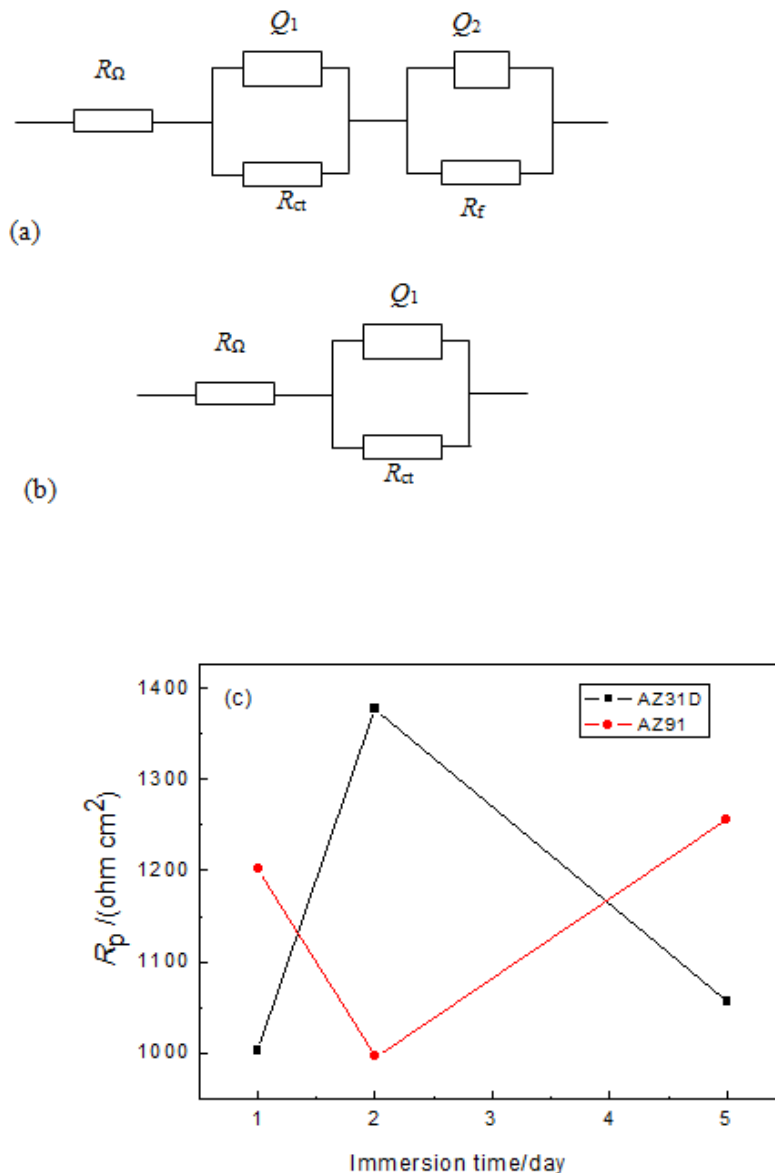


Figure 9. The equivalent circuit was used for fitting EIS data with two capacitive loops(a) and one capacitive loops(b) present in the plots of AZ31D and AZ91 Mg alloys and the polarization resistance (R_p)(c) of AZ91 and AZ31D Mg alloys after immersion in the *m*SBF for 1d, 2 d and 5d.

Table 4. Results of EIS curves of three kinds of samples after immersion in the *m*-SBF for 1d, 2d and 5d.

| Sample | AZ31D | | | AZ91 | | |
|--------------------------------|-------|------|------|------|-----|------|
| | 1d | 2d | 5d | 1d | 2d | 5d |
| $R_{ct} / (\Omega\text{cm}^2)$ | 433 | 486 | 839 | 420 | 320 | 461 |
| $R_f / (\Omega\text{cm}^2)$ | 570 | 891 | 218 | 781 | 676 | 795 |
| $R_p / (\Omega\text{cm}^2)$ | 1003 | 1377 | 1057 | 1201 | 996 | 1236 |

Fig. 10 and Table 5 show the Tafel plots of AZ31D and AZ91 Mg alloys after immersion in the *m*SBF for different days. The corresponding electrochemical parameters extracted from these curves are given in Table 5. From Fig. 10, it could be observed that the corrosion potential E_{corr} values of AZ31D shifted in the negative direction and the i_{corr} and CR* of AZ31D decreased steadily. Compared with AZ31D, it could be observed that the E_{corr} values of AZ91 shifted to the positive direction after immersed in the *m*SBF from 8d to 24 d. And its i_{corr} was first decreased slowly and then increased rapidly and the biodegradable rate showed the same tendency. Compared with corrosion rate calculated from these two methods, it could be observed that that the tendency was a little different and CR from mass loss was much faster than that from electrochemical parameters.

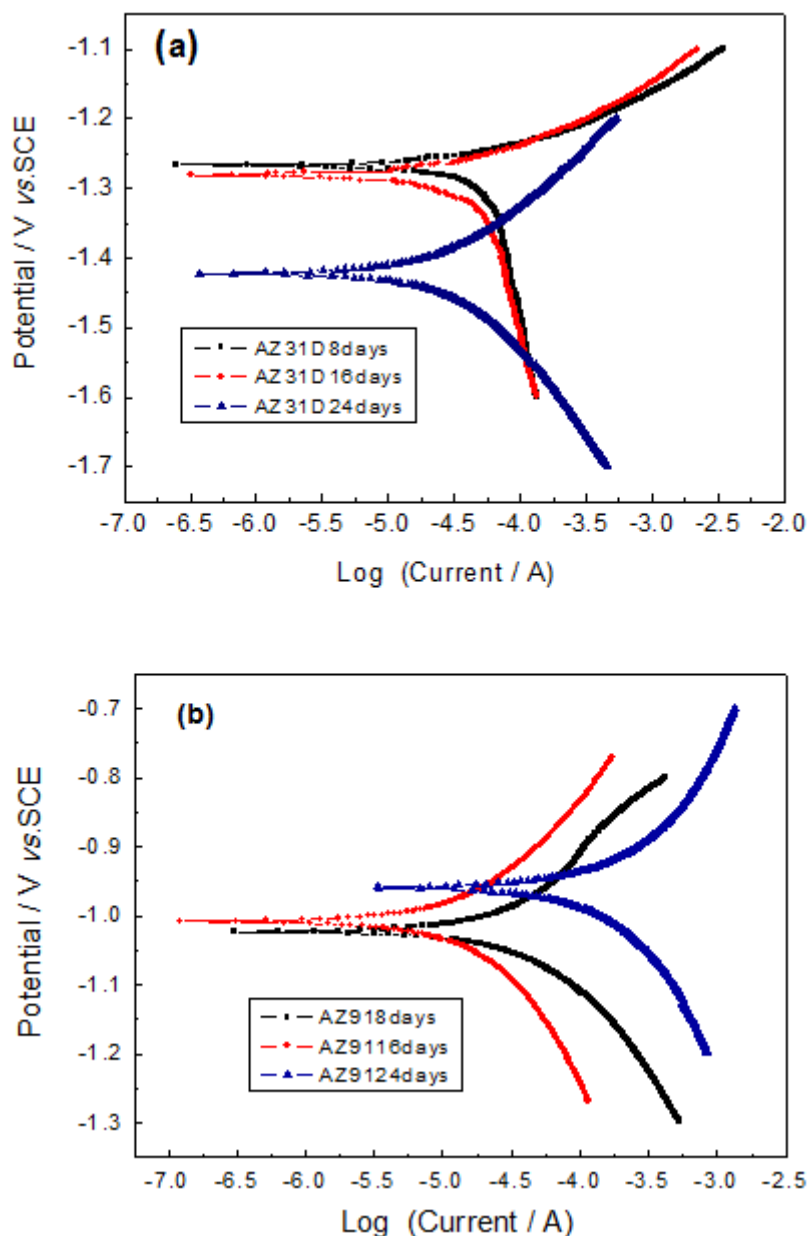


Figure 10. Tafel plots of AZ31D(a) and AZ91(b) Mg alloys after immersion in the *m*SBF for 8d, 16d, 24d.

Table 5. Results of Tafel plots of three kinds of samples after immersion in the m-SBF for 8d,16d and 24 d.

| Sample | AZ31D | | | AZ91 | | |
|--------------------------------------|----------|-----------|-----------|----------|----------|----------|
| | 8d | 16d | 24d | 8d | 16d | 24d |
| $E_{\text{corr}}/V(\text{ vs.SCE})$ | -1.268 | -1.282 | -1.422 | -1.023 | -1.008 | -0.959 |
| $i_{\text{corr}}/(A\text{ cm}^{-2})$ | 5.334e-5 | 4.340 e-5 | 2.424 e-5 | 3.625e-5 | 1.459e-5 | 2.005e-4 |
| $CR^*/(\text{mm yr}^{-1})$ | 0.1191 | 0.0969 | 0.0541 | 0.0809 | 0.0325 | 0.4475 |
| $CR/(\text{mm yr}^{-1})$ | 2.5203 | 2.6666 | 1.6360 | 1.6932 | 1.2702 | 0.8858 |

CR* calculated according to equation (2) from electrochemical parameters and CR from mass loss.

3.3. Corrosion mechanism

The biodegradable behavior and electrochemical behavior of AZ31D and AZ91 was significantly influenced by the following factors, such as the composition of the alpha-Mg matrix, the composition of the other phases, the distribution of the other phases and the composition of the immersion solution [19]. When AZ31D and AZ91 Mg alloy specimens were exposed into mSBF, Mg elements first dissolved and corrosion layers formed according to the following reactions (Eq.(3)-(5)):



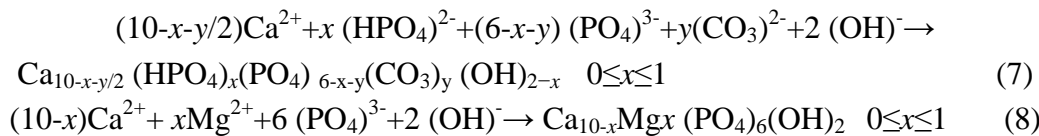
With time increased, further anodic reaction would result in more dissolution of Mg^{2+} in the mSBF with more consumption of HCO_3^- and HPO_4^{2-} which caused an increase in the Cl^- concentration [26]. The Cl^- ion could therefore easily penetrate the deposition layer due to its small radius causing the preferential adsorption and the OH^- replacement by the Cl^- [20,21]. And then $\text{Mg}(\text{OH})_2$ converted to more soluble MgCl_2 , and the dissolution of $\text{Mg}(\text{OH})_2$ made the surface more active, decreased the protected area and promoted further dissolution of magnesium. The reactions were summarized as followed (Eq.(6)):



During Mg grains were corroded, the precipitates would be in the top layer in pitting initiation. These could increase in the number of active atoms on the surface, accelerating the formation of the protective layers (Fig. 1). The elements of Ca, P, Mg, Al and O were observed in the deposit layers (Fig. 2-3). EDX mapping observed that Ca, P, Mg, Al and O were homogeneously distributed in the corrosion layers of AZ31D, while, inhomogeneously distributed in AZ91. This indicated that the surface partially protective film would lower the influence of micro-galvanic corrosion and an extra resistance produced between the α Mg phase and the second phase became an effective driving force to decrease the micro-galvanic corrosion [22].

Thermodynamics predicted that as the reaction progressed, the high amount of Mg^{2+} subsequently reacted with phosphate ions (HPO_4^{2-} or PO_4^{3-}), HCO_3^{2-} , OH^- and Ca^{2+} in the solution to form amorphous calcium phosphate or magnesium calcium apatite ($\text{Ca}_{10-x}\text{Mg}_x(\text{PO}_4)_6(\text{OH})_2$) due to the solubility product of HA ($K_{\text{sp}}(\text{HA}) = 2.35 \times 10^{-118}$) were much greater than that of $\text{Ca}_3(\text{PO}_4)_2$

($K_{sp}(\text{Ca}_3(\text{PO}_4)_2) = 2.0 \times 10^{-29}$), $\text{Mg}_3(\text{PO}_4)_2$ ($K_{sp}(\text{Mg}_3(\text{PO}_4)_2) = 1.04 \times 10^{-24}$), $\text{Mg}(\text{OH})_2$ ($K_{sp} \text{Mg}(\text{OH})_2 = 1.8 \times 10^{-11}$) at 37 °C(Eq.(7)-(8)).



Which was in accordance with previous studies [23,24]. When Mg was exposed to a supersaturated solution containing Ca^{2+} , H_2PO_4^- and HPO_4^{2-} ions like Hank's solution, hydroxyapatite, heavily carbonated apatite and slightly carbonated apatite would precipitate. In this study, the inductive loop emerged in the low-frequency was assumed to be the formation of the $\text{Mg}(\text{OH})_2$ and/or MgO [25] (Fig.8) and also to the formation and precipitation of an insoluble phosphates and carbonates film[26,27-33]. Typically Ca/P atomic ratios can be used to determine the nature of a particular calcium phosphate phase: Calcium hydrogen phosphate (CaHPO_4) = 1.0, octacalcium phosphate ($\text{Ca}_8\text{H}_2(\text{PO}_4)_6\text{H}_2\text{O}$) = 1.33, tricalcium phosphate ($\text{Ca}_3(\text{PO}_4)_2$) = 1.5, HA($\text{Ca}_{10}(\text{PO}_4)_6(\text{OH})_2$) = 1.67[34]. In this study, the Ca/P ratio was lower than 1.3(Fig.4) and many small peaks were present in the 2θ range between 20–35° (Fig.5), which might verify that the amorphous calcium phosphate phases might form on the surfaces of the samples[35-37].

In addition to the possible enhancement of cell attachment and growth, the precipitation of calcium phosphates on the surface may slow down the dissolution of magnesium due to the formation of compact and insoluble phosphates[23] (Fig(1-5)). Unlike $\text{Mg}(\text{OH})_2$, the precipitated phosphates not only could not be destroyed by chloride ions but also could reduce the permeability of Ca^{2+} and PO_3^{4-} ions in the interface between the corrosion layer and the Mg alloy substrate. So, Ca^{2+} and PO_3^{4-} ions were mainly in the corrosion medium and the surfaces of corrosion layer [38] (Fig.(1-5)). And the corrosion rates were slower from 8d to 24d than that from 1d to 5d (Fig. 7).

From the results of immersion test and electrochemistry test, it could be observed that the corrosion rate of AZ31D was faster than that of AZ91(Fig.7-8 and Table 5). The main reason might be as followed. The intermetallic of AZ91 mainly consisted of $\beta\text{-Mg}_{12}\text{Al}_{17}$ phase, While, AZ31D possessed possible Al–Mg–Mn compounds which might be $\beta\text{-Mg}_{12}\text{Al}_{17}$ and Al_8Mn_5 phase (Fig. 6 and Table 3). The much more β -phase and inhomogeneously distribution in AZ91 make the micro-galvanic couple form at the boundaries between the β phase and Mg matrix to accelerate the α phase corrosion(Fig.2 and Fig.6). With time increased, the remained β phases of AZ91 form a continuous distribution which could form a tight barrier, and the corrosion of Mg matrix was difficult to traverse this barrier (Fig.6). So, some micro-pores observed in AZ91 alloys due to the continuous β phases effectively inhibit the propagation of corrosion (Fig.1). Compared with AZ91, AZ31D possessed much less Al and a little more Mn which were well-distributed and showed much different corrosion appearances(Fig.6 and Fig.6). The grain boundary of AZ31 was not a tight corrosion barrier like AZ91 that can retard the development of corrosion, and corrosion does not stop at grain boundaries; instead, corrosion slightly preferential occurs along grain boundaries which was in accordance with other work[39-40](Fig.6). The main reason might be that the presence of Al–Mg–Mn compounds in a grain boundary could be regarded as a wall made of dislocations between grains which were believed to be more susceptible to corrosion attack [41-42]. It was reported that the potential of Al_8Mn_5 was

about 200–250 mV more positive than that of the Mg–Al matrix[43] and the potential value of Al_8Mn_5 was 250–350 mV \pm 90 mV for this intermetallic than those of $\text{Mg}_{17}\text{Al}_{12}$ being 60–150 mV \pm 20 mV [44–46]. So, a local galvanic effect accelerated the dissolution of the area near the Al–Mg–Mn compounds due to their more positive corrosion potentials [47]. Corrosion products mainly consisted of Mg oxides or hydroxides with some alloy composition, such as Al, Zn and Mn (Fig.3).

In this study, the electrochemical EIS measurements showed that R_{ct} reflected how difficult the electrochemical corrosion reaction could be and R_f corresponds to the relaxation of mass transport through the corrosion product layer [48]. R_p can be calculated from the equivalent circuits by adding R_{ct} and R_f which suggested that AZ91 exhibited a higher degradation resistance than that of AZ31D at immersion time being 1d and 5d while lower one being 2d which might be due to the corrosion layers detached. It has a known issue that the corrosion rate based on the electrochemical measurements do not agree with direct measurements using weight loss [8,49]. This study verified this results. The Tafel experiment showed the E_{corr} values of AZ91 tended to corrosion resistance and AZ31D tended to corrosion which was in accordance with the direct measurements using weight loss (Table 5, Fig.7-9 and Fig.11). However, most importantly, the E_{corr} only represented the thermodynamics tendency while i_{corr} was always regarded as an indication of the velocity of uniform corrosion. With immersion time increased the i_{corr} of AZ31D decreased which meant that the corrosion resistance became increased and the biodegradable rate decreased, which was in agreement with the results of the immersion test (Table5 and Fig.8-9). While, The i_{corr} and the biodegradable rate of AZ91 Mg alloy was not in accordance with the results of the immersion test (Table 5 and Fig.7-9). The main reason might be that Tafel plots could be employed to study the corrosion rate of the uniform corrosion attack instead of non uniform corrosion and a defects quantification approach was proposed by calculating the relation of the defects (pores) area to the total analyzed area [49]. Other studies thought that there might be more than one cathodic reaction in the cathodic branch of the polarisation curve even though there appears to be a linear “Tafel” region and the corroding area might be different during solution immersion which result in different electrochemical reactions and then the measurement of the polarisation curve might be different, either [8].

4. CONCLUSIONS

In a modified simulated body fluid (*m*SBF), a more protective surface film made the corrosion rate (CR) decrease to a stable stage with immersion time increasing from 1d to 24d. CR of AZ91 was significantly lower than that of AZ31D. Much more β -phase inhomogeneously distributed in AZ91 and little β -phase well-distributed in AZ31D, so, Ca, P, Mg, Al and O were homogeneously distributed in the corrosion layers of AZ31D, while, inhomogeneously in AZ91. With immersion time increased, the left β phases of AZ91 gradually formed a tight barrier while a loosen one were in AZ31D. Scanning electron microscopy (SEM) with energy dispersive spectroscopy (EDS) and X-ray diffraction (XRD) analysis verified that amorphous calcium phosphate or magnesium calcium apatite has formed on the surfaces of AZ91 and AZ31D.

ACKNOWLEDGEMENTS

This work was supported by the Natural Science Foundation of China (No.51272058 and No. 51042012) and the Hospital Foundation of First Affiliated Hospital of Harbin Medical University.

References

1. X. Gu, Y. Zheng, Y. Cheng, S Zhong and T. Xi, *Biomaterials.*, 304(2009)484.
2. G. Song, *Adv. Mater. Res.*,29–30 (2007) 95.
3. M.P. Staiger, A.M. Pietak, J. Huadmai and G. Dias,*Biomaterials*, 27 (2006) 1728.
4. G. Song and S. Song, *Acta Phys. Chim. Sin.*, 22 (2006) 1222.
5. A. Pardo, M.C. Merino, A.E. Coy, F.Viejo, R. Arrabal, and S. Feliú, *Electrochim. Acta.*, 53 (2008) 7890 .
6. G. Ben-Hamu, D. Eliezer, K.S. Shin and Cohen S, *J. Alloys. Compd.*, 431(2007)269.
7. N. Aung and W. Zhou. *Corros.Sci.*,53(2010) 589.
8. G. Song, *Corros. Sci.*,7 (2005) 563.
9. W.C. Neil, M. Forsyth, P.C. Howlett. C.R. Hutchinson and B.R.W. Hinton, *Corros.Sci.*,51 (2009) 387.
10. R. Ambat, N.N. Aung and W. Zhou, *Corros.Sci.*,42(2000)1433.
11. Z.H. Wen, C.J. Wu, C.S. Dai and F.X. Yang, *J. Alloys. Compd.*, 488(2009)392.
12. ASTM B 275-90:American Society for Testing and Materials, Philadelphia, Pennsylvania, USA, 1990.
13. T. Kokubo and H. Takadama. *Biomaterial*, 27(2006)2907.
14. ASTM-G31-72: Standard Practice for Laboratory Immersion Corrosion Testing of Metals. Annual Book of ASTM Standards.
15. M.M. Avedesian, H. Baker (Eds.), Magnesium and Magnesium Alloys, ASM International, Material's Park, OH, 1999.
16. F. Zucchi, V. Grassi, A. Frignani, C. Monticelli and G. Trabanelli,*Surf.Coat.Technol.*,36(2006) 4136.
17. T. Zhang, Y.W. Shao, G.Z. Meng, Z.Y. Cui and F.H. Wang. *Corros.Sci.*,53(2011)1960.
18. N. Aung and W. Zhou, *Corros.Sci.*,53(2010) 589.
19. Z.M. Shi, M. Liu and A. Atrens, *Corros.Sci.*,52(2010)579.
20. L. Wang, B.P. Zhang and T. Shinohara, *Mater and Desig.*,31(2010)857.
21. J.Wang, L. Wang, S. Guan, S. Zhu, C. Ren and S. Hou, *J. Mater. Sci. Mater. Med.* 21(2010) 2001.
22. N.I.Z. Abidin, D. Martin and A. Atrens, *Corros.Sci.*, 53 (2011) 862.
23. L.Yang and E. Zhang, *Mater. Sci. Eng. C*,29(2009)1691.
24. H. Kuwahara, Y. Al-Abdullat, N. Mazaki, S. Tsutsumi and T. Aizawa, *Mater. Trans.* 42(2001) 1317.
25. K.Y. Chiu, M.H. Wong, F.T. Cheng and H.C. Man. *Surf. Coat.Technol.*, 202(2007) 590.
26. M. Yang, L.Cheng and F. J. Pan, *Mater. Sci.*, 44(2009)4577.
27. B. Breslin and L. Rudd, *Corros.Sci.*, 42(2000)1023.
28. L. Mueller and F.A. Mueller, *Acta. Biomater.*2(2006)181.
29. Y.C. Xin, C.L. Liu, X.M .Zhang, G.Y. Tang, X.B. Tian and P.K. Chu, *J. Mater.Res.*,22(2007)2004.
30. Y.C. Xin, T. Hu and P.K.Chu, *J. Electrochem. Soc.*57(2010)C238.
31. Y.C. Xin, K.F. Huo, T. Hu, G.Y. Tang, P.K. Chu, *J. Mater. Res.*,24(2009)2711.
32. F. Witte, V. Kaese, H. Haferkamp, E. Switzer, A. Meyer-Lindenberg, C.J. Wirth and H. Windhagen, *Biomaterials*,26(2005)3557.
33. L. Li, J. Gao and Y. Wang. *Surf.Coat.Technol.*,185(2004)92.
34. S. Shadanbaz and G.J. Dias. *Acta. Biomater.*, 8(2012)20.

35. Z. Li, X. Gu, S. Lou and Y. Zheng. *Biomaterials*, 29(2008)1329.
36. H.R. Bakhsheshi-Rad, M.R. Abdul-Kadir, M.H. Idris an S. Farahany. *Corros.Sci.*, 64(2012)184.
37. J.Yongseok, C.Boyce, S. Jagannathan and Y. Yeoheung. *Acta. Biomater.*, 9(2013) 8761.
38. Y. Xin, T. Hub and P.K. Chu, *Acta. Biomater.*, 7(2011)1452.
39. G.L. Song , R. Mishra, Z.Q. Xu, *Electrochem Commun*, 12 (2010) 1009.
40. G.L.Song and Z.Q. Xu, *Electrochim. Acta.*, 2010; 55:4148.
41. G. Ben-Hamu, D. Eliezer and L. Wagner, *J. Alloys. Compd.*, 468(2009) 222.
42. G. Song and A. Atrens, *Adv. Eng. Mater.*, 5(2003)837.
43. G.L. Song and Z.Q. Xu, *Corros.Sci.*, 54 (2012) 97.
44. F. Andreatta, I. Apachitei, A.A. Kodentsov, J. Dzwonczyk and J. Duszczyk, *Electrochimic. Acta.* 51 (2006) 3551.
45. M.Ben-Haroush, G. Ben-Hamu, D. Eliezer and L.Wagner, *Corros.Sci.*, 50 (2008) 1766.
46. M. Liu and G.L. Song. *Corros.Sci.*, 77 (2013) 143.
47. M. Jösön, D. Thierry and N. LeBozec, *Corros.Sci.*, 48(2006)1193.
48. J.X. Jia, A. Atrens, G. Song, and T.Muster. *Mater Corros.*, 56(2005)468.
49. M. Bockmeyer and P. Löbmann, *Thin Solid Films* 515(2007)5212.

© 2014 The Authors. Published by ESG (www.electrochemsci.org). This article is an open access article distributed under the terms and conditions of the Creative Commons Attribution license (<http://creativecommons.org/licenses/by/4.0/>).